ACS central science

http://pubs.acs.org/journal/acscii

Research Article

Highly Efficient Photo-/Electrocatalytic Reduction of Nitrogen into Ammonia by Dual-Metal Sites

Shiyan Wang, Li Shi, Xiaowan Bai, Qiang Li, Chongyi Ling, and Jinlan Wang*

Cite This: *ACS Cent. Sci.* 2020, 6, 1762–1771

Read Online

ACCESS | Metrics & More | Article Recommendations | Supporting Information

ABSTRACT: The photo-/electrocatalytic nitrogen reduction reaction (NRR) is an up and coming method for sustainable NH_3 production; however, its practical application is impeded by poor Faradaic efficiency originating from the competing hydrogen evolution reaction (HER) and the inert N≡N triple bond activation. In this work, we put forth a method to boost NRR through construction of donor−acceptor couples of dual-metal sites. The synergistic effect of dual active sites can potentially break the metal-based activity benchmark toward efficient NRR. By systematically evaluating the stability, activity, and selectivity of 28 heteronuclear dual-atom catalysts (DACs) of M1M2/g-C_3N_4 candidates, FeMo/g-C_3N_4 is screened out as an effective electrocatalyst for NRR with a particularly low limiting potential of −0.23 V for NRR and a rather high potential of −0.79 V for HER. Meanwhile, TiMo/g-C_3N_4, NiMo/g-C_3N_4, and MoW/g-C_3N_4 with suitable band edge positions and visible light absorption can be applied to NRR as photocatalysts. The excellent catalytic activity is attributed to the tunable composition of metal dimers, which play an important role in modulating the binding strength of the target intermediates. This work may pave a new way for the rational design of heteronuclear DACs with high activity and stability for NRR, which may also apply to other reactions.

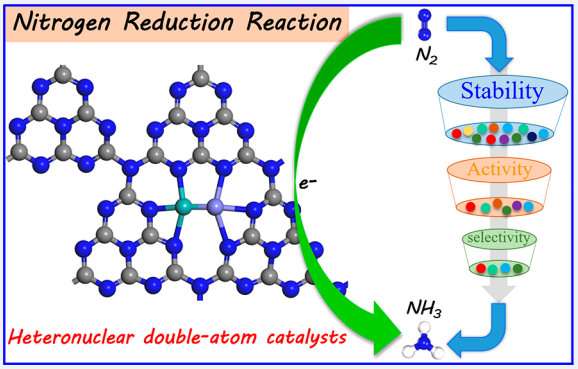

1. INTRODUCTION

An essential chemical in contemporary life is ammonia (NH_3), which has been widely used in agriculture, industry, and as a household chemical.[1−3] While the Haber−Bosch process is the primary source for the nitrogen (N_2) reduction reaction (NRR) on the industrial-scale, a photo-/electrochemical method to bring the conversion of N_2 into NH_3 under milder conditions represents an attractive alternative. By using water as a proton donor in the photo-/electrocatalytic NRR, reliance on natural gas in conventional NH_3 synthesis can be reduced, resulting in reduced carbon dioxide (CO_2) emission.[4−9] However, the high activation energy that is required to break the strong N≡N bond as well as the weak adsorption of nonpolarized N_2 onto catalysts are two major challenges in the NRR.[10,11] The ideal solution for this process requires a suitable catalyst to ensure a high reaction rate and selectivity, which remains a salivating goal.

Transition metal single-atom catalysts (SACs), a new class of catalysts, have recently been demonstrated to exhibit superior catalytic performances for NRR.[12−16] However, it is still rather challenging for SACs to simultaneously improve the Faradaic efficiency and the yield rate. A promising strategy to address this issue is to introduce dual-metal sites to tune the adsorption property of the targeted intermediates. Double-atom catalysts (DACs), especially heteronuclear DACs, with synergetic interatomic interactions and flexible active sites, can maximize the potentials of SACs for multistep reactions, which makes the optimization of activity and selectivity feasible. For example, NiMn and NiCu anchored on g-C_3N_4 were found to suppress the competing HER more efficiently than their monometallic counterparts and therefore delivered high Faradaic efficiency and selectivity for the CO_2 reduction reaction (CO_2RR) into CO.[17] The CuAu/g-C_3N_4 bimetallic photocatalyst could efficiently catalyze the hydroxylation of benzene via C−H activation under visible light irradiation.[18] Heteronuclear dual metals (CoPt, FeCo, ZnCo) embedded on N-doped carbon enhanced the binding ability of oxygen (O_2) and facilitated the activation of O═O bond, which were served as efficient O_2 reduction reaction (ORR) catalysts with outstanding activity.[19−24] In particular, NiCo heteronuclear dimer anchored on g-C_2N exhibited higher catalytic activity toward CO_2RR into CH_4 than CoCo and NiNi homonuclear dimers.[25] For NRR, several heteronuclear metal-dimers anchored on N-doped graphene and phthalocyanine were proposed to have an

Received: May 2, 2020
Published: September 21, 2020

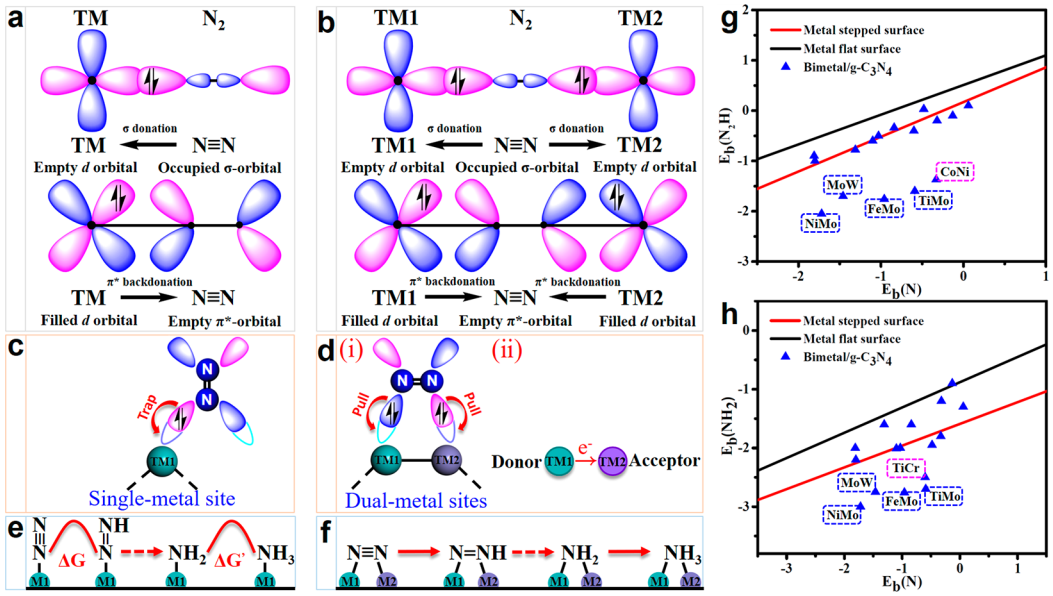

Figure 1. Simplified schematic diagram showing N_2 bonding to (a) single metal and (b) dual metals M1/g-C_3N_4 and M1M2/g-C_3N_4, respectively. The capture and activation of N_2 on (c) single-metal site, and (d) dual-metal sites through the pull−pull effect. (e) Schematic depiction of high Gibbs free energy change attributed to the inherent linear scaling relations between the binding energies of *N versus *N_2H, *N versus *NH_2 on M1/g-C_3N_4. (f) Reducing the free energy change by deviating above scaling relation on M1M2/g-C_3N_4. Binding energies (g) E_b(N) versus E_b(N_2H) and (h) E_b(N) versus E_b(NH_2) for g-C_3N_4 supported heteronuclear dual-metals, as well as the transition-metal scaling relations.

improved catalytic activity than the corresponding homonuclear DACs.[26,27] Very recently, Chen et al.[28] obtained a NRR Faradaic efficiency up to 67.8% by constructing donor−acceptor couples of Au and Ni nanoparticles on N-doped carbon. The donor−acceptor couples can enhance the preadsorption of N_2 and decrease the energy of desorption of NH_3 on electron-rich surface of Au simultaneously. Therefore, design of heteronuclear DACs by constructing multiple active centers with correlative interactions is a potential strategy for improving the activity of many chemical reactions.

This work depicts that heteronuclear metal dimers embedded in g-C_3N_4 as a dual metal active center can generate donor−acceptor couples and significantly boost the activity and selectivity for NRR. By comparing the thermodynamic and electrochemical stabilities of 28 candidates of M1M2/g-C_3N_4, we first screen out 16 heteronuclear DACs that meet the stability criteria for further investigation. Subsequently, we systematically evaluate the catalytic activity by studying the scaling relations of E_b(N) vs E_b(N_2H) and E_b(N) vs E_b(NH_2), FeMo, TiMo, MoW, and NiMo dimers are selected out as promising DACs for NRR. Finally, by comparing the potential determining step and limiting potential of above DACs, FeMo/g-C_3N_4 is highlighted for NRR with a relatively low negative limiting potential of −0.23 V through the enzymatic mechanism. Meanwhile, TiMo/g-C_3N_4, MoW/g-C_3N_4, and NiMo/g-C_3N_4 possess suitable band gaps and band edge positions, allowing the reduction reaction to occur under visible light. The high activity stems from heteronuclear metal dimers and g-C_3N_4 acting synergistically, which not only serves as a coordination skeleton but also provides a favorable local environment for NRR. Furthermore, the proposed model of donor−acceptor couples of heteronuclear dual-metals for N_2 activation can be extended to other systems such as FeMo-doped graphene for achieving high-efficiency NRR.

2. RESULTS AND DISCUSSION

The graphitic carbon nitride (g-C_3N_4) monolayer possesses evenly distributed holes,[29] which provide uniform and abundant nitrogen coordination sites with electron-rich lone pairs for capturing metals.[13,30] In fact, the ultrathin material offers other inherent advantages as a substrate to attach metal catalysts such as keeping metal atoms in their neutral state, effective accumulation of surface polarization charges on metal atoms, and providing reliable and useful information in terms of identification of catalytically active sites. In addition, the layered g-C_3N_4 is proven to be a potential photocatalytic material with a suitable band gap and has been extensively used in energy conversions with visible light.[31,32] Meanwhile, the large periodic holes of s-heptazine can provide sufficient space for supporting heteronuclear metal dimers tightly by sp^2-bonded N atoms;[33,34] thus, the s-heptazine g-C_3N_4 is used as the substrate in this work.

According to the "acceptance-donation" mechanism,[5,27] single metal atom and dual-metal sites with empty d-orbitals can accept lone-pair electrons of N_2, and the partially filled d-electrons donate electrons back to the antibonding orbitals of the adsorbed molecule; thus, the N≡N triple bonds are weaken and activated (Figure 1a,b). However, the empty d-orbital of a single-metal site can trap one lone pair electron of one side of the N_2 molecule (Figure 1c). To maximize the activation process, the empty d-orbitals of the dual-metal sites can pull two lone pair electrons at both ends of N_2 (Figure 1d). As discussed above, the incorporation of heteronuclear dual-metals provides an alternative strategy to get adjacent active sites and thus increase the binding strength of the targeted intermediates. In addition, the donor−acceptor couples of heteronuclear dual-metals (i.e., the synergistic effect from M1 and M2) lead to a polarized surface with multielectron sites and promote the activation of the nonpolarized N_2 molecule (Figure 1d). With the help of the dual-metal sites, it can also be expected that the inherent linear scaling relations limited by

https://dx.doi.org/10.1021/acscentsci.0c00552
ACS Cent. Sci. 2020, 6, 1762−1771

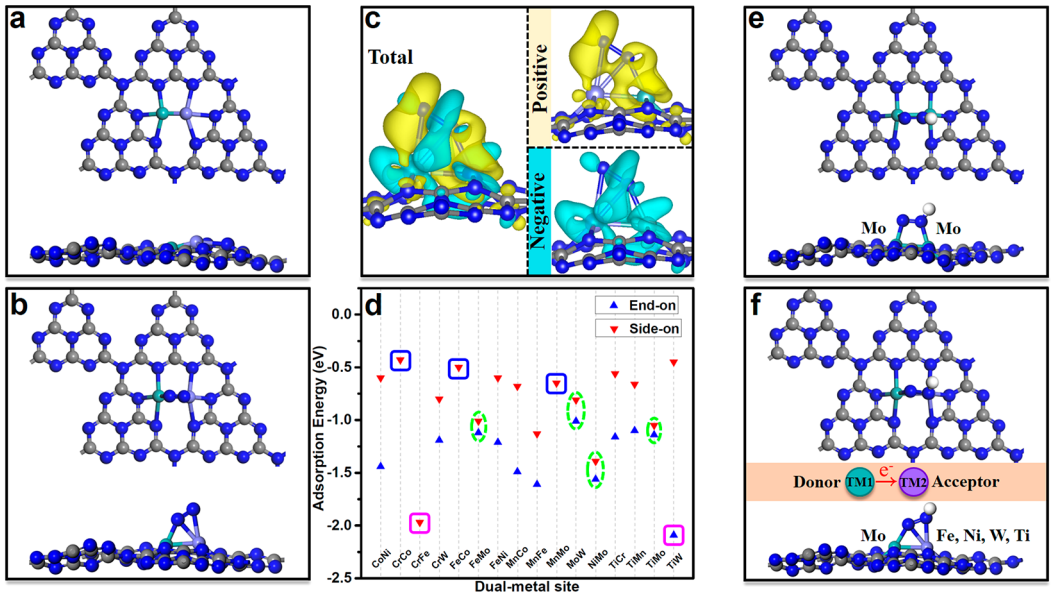

Figure 2. Optimized structure of (a) M1M2/g-C_3N_4 and (b) adsorption of N_2 on M1M2/g-C_3N_4. (c) Charge density difference for N_2 adsorption on M1M2/g-C_3N_4, where yellow and cyan show the positive and negative charges, respectively. The isosurface value is 0.001 e/Å^3. (d) Adsorption energies of N_2 on M1M2/g-C_3N_4 with the end-on and side-on pattern. Green circles mark the cases with mild adsorption strengths and small differences of adsorption energies via both side-on and end-on pattern adsorption of N_2, blue squares have much low adsorption energies and pink squares have very large adsorption energies. Optimized structures of adsorption of *N_2H intermediates on (e) MoMo/g-C_3N_4 and (f) M1M2/g-C_3N_4. The C, N, and H atoms are labeled as gray, blue, and white balls, respectively.

a single metal site can be broken. As shown in Figure 1e, the large changes in Gibbs free energy can be attributed to the linear scaling relations between the binding energies of *N versus *N_2H, *N versus *NH_2 on the single-metal site.[13] Additional N-binding sites are needed for the stabilization of N-containing intermediates in order to reduce the large changes in Gibbs free energy of the potential determining step (PDS). We expect that constructing the donor−acceptor couples of dual-metal sites will break the inherent linear scaling relations, thus causing the PDS to decrease dramatically (Figure 1f).

Nonprecious metals including Cr, Ti, Fe, Mn, Co, Mo, Ni, and W, which have been widely used as single-atom catalysts to catalyze NRR,[13,30,35] are considered in this work. The feasibility of 28 types of dual-metals (two out of Cr, Ti, Fe, Mn, Co, Mo, Ni, and W are taken in combination to form heteronuclear dual-metals, i.e., TiCr, TiMn, TiFe, TiCo, TiNi, TiMo, TiW, CrMn, CrCo, CrFe, CrMo, CrNi, CrW, MnCo, MnFe, MnNi, MnMo, MnW, FeNi, FeCo, FeMo, FeW, CoNi, CoMo, CoW, NiMo, NiW, and MoW dimer) deposited on the g-C_3N_4 and affixed by N-coordination sites around the inherent cavities was investigated. We first evaluated the stability of the metal dimers incorporated into the g-C_3N_4 substrate; the energy difference (ΔE) between the adsorption (E_b) of metal dimers on g-C_3N_4 and the cohesive energy (E_{coh}) of TM atoms in their metal crystals is used to estimate the stability of C_3N_4-supported metal dimers.[36,37] When $\Delta E < 0$, it indicates that metal dimers being uniformly embedded in g-C_3N_4 are more favored energetically than forming the metal bulk. As shown in Figure S1, 16 promising candidates (i.e., the C_3N_4-supported TiCr, TiMn, TiMo, TiW, CrFe, CrCo, CrW, MnFe, MnCo, MnMo, FeCo, FeNi, FeMo, CoNi, NiMo, and MoW dimers) with negative ΔE values are determined. Therefore, they are expected to form stable heteronuclear metal dimers rather than aggregating into clusters anchored on the g-C_3N_4 monolayer. Calculation of the dissolution potential (U_{diss}, versus SHE) was performed to further evaluate the electrochemical stabilities of heteronuclear DACs. According to the definition (see Supporting Information), a positive value ($U_{diss} > 0$ V vs SHE) indicates the strong binding of the dual metals with the substrate. As shown in Table S1, TiCr, TiMn, TiMo, TiW, CrMn, CrFe, CrCo, CrW, MnFe, MnCo, MnNi, MnMo, MnW, FeCo, FeNi, FeMo, CoNi, NiMo, and MoW anchored in g-C_3N_4 possess positive U_{diss} values, implying that they are energetically stable. Finally, 16 DACs are screened out that meet the stability criteria for further investigation.

Generally, the potential-limiting step of NRR is either $N_2 \rightarrow N_2H$ or $NH_2 \rightarrow NH_3$,[38] thus the binding energies of *N [E_b(N)], *N_2H [$E_b(N_2H)$] and *NH_2 [$E_b(NH_2)$] determine the overall reaction rate in most cases. Earlier DFT studies have revealed that the poor activity with high NRR limiting potential originates from the inherent linear scaling relations of E_b(N) vs $E_b(N_2H)$ and E_b(N) vs $E_b(NH_2)$ on the pure transition metal (TM) based catalysts surfaces[39,40] and single-atom metal catalysts,[13] averting them to approach optimal NRR activity region. Therefore, a successful catalyst design must circumvent or even break this limitation to achieve high NRR activity. Several strategies have been proposed to circumvent the linear scaling relations of the adsorbed surface intermediates.[36] Typically, Wang et al.[41] showed that by intervening in the TM-mediated catalysis with a second catalytic site, the scaling relations could be broken. On the basis of this, we further calculated the adsorption of *N, *N_2H, and *NH_2 on g-C_3N_4 supported metal dimers. As shown in Figure 1g,h, four heteronuclear DACs of TiMo/g-C_3N_4, NiMo/g-C_3N_4, FeMo/g-C_3N_4, and MoW/g-C_3N_4 can break the scaling relation of the transition metal surface[39,40] and effectively optimize the adsorption properties of NRR intermediates, which are expected to achieve improved NRR activity.

https://dx.doi.org/10.1021/acscentsci.0c00552
ACS Cent. Sci. 2020, 6, 1762−1771

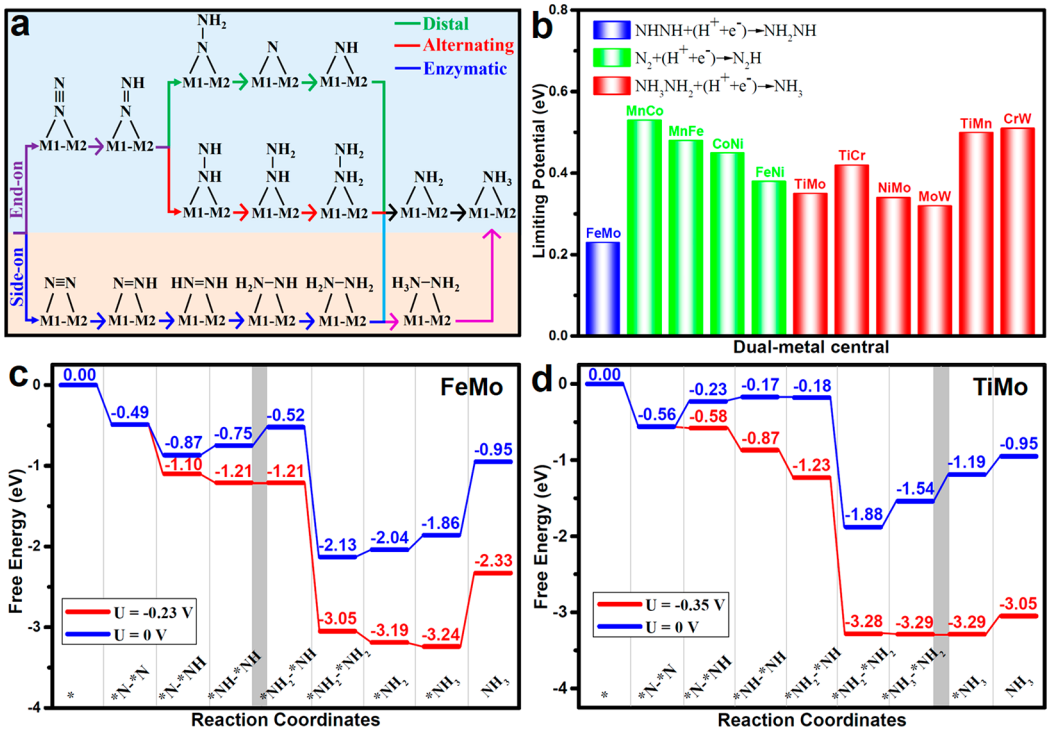

Figure 3. (a) Schematic depiction of three reaction mechanisms for NRR on M1M2/g-C_3N_4. (b) Limiting potentials for NRR on M1M2/g-C_3N_4. ("$H^+ + e^-$" represents to proton coupled electron transfer process.) Free energy diagrams for NRR on (c) FeMo/g-C_3N_4 and (d) TiMo/g-C_3N_4 at different applied potentials. Here, * denotes a catalytic active site.

Figure 2a shows the optimized structures of M1M2/g-C_3N_4; the metal dimers are anchored on porous g-C_3N_4, in which there is strong coordination of each dispersed metal atom with the other metal atom as well as three N atoms, forming N-coordinated N_3M1-M2N_3 configuration. Figure 2b presents the structures of N_2 adsorbed on M1M2/g-C_3N_4, the dual-metal sites act as *N binding. To gain a deep insight into the interaction between the N_2 and M1M2, the charge density difference is further calculated. As evident from Figure 2c, the charge transfer process between the anchored M1M2 and the adsorbed N_2 is bidirectional, and the charge accumulation and depletion can be found on both sides. These characteristics are in good agreement with the donation/back-donation picture (Figure 1b); i.e., dual-metal catalysts can "push" electrons into the N_2 antibonding orbitals and "pull" the N_2 lone-electrons pair, which can activate N_2, leading to the significant increase in elongation of N≡N bond (1.20−1.24 Å, vs 1.12 Å in the free gas phase).

In the following, the adsorption energies of N_2 on M1M2/g-C_3N_4 (Figure 2d) are calculated via both the end-on and side-on patterns. Our results show that the N_2 prefers to attach the dual-metals with an end-on configuration, and the adsorption energies range from −1.01 to −2.09 eV. Notably, the moderate adsorption strengths and small differences of adsorption energies via both side-on and end-on adsorption of N_2 on FeMo, MoW, NiMo, and TiMo (green circles) suggest that these four catalysts can be good NRR catalysts (Figure S2). On the contrary, the adsorption energies of N_2 on CrCo, FeCo, and MnMo (blue squares) are very low (∼ −0.50 eV), implying that they are not suitable for N_2 fixation. In addition, the excessively strong adsorption strength of N_2 (∼ −2.00 eV) on CrFe and TiW (pink squares) signifies that the desorption step of *NH_3 is difficult in the meantime. As for the end-on manner, the N_2 adsorption on CrCo, FeCo, and MnMo dimer sites is unstable and spontaneously optimizes to side-on configuration.

To gain a better understanding of the effect of donor−acceptor couples of dual-metal sites on NRR, the structure of *N_2H on homonuclear and heteronuclear metal dimers is compared and shown in Figures 2, panels e and f, respectively. Clearly, the first hydrogenation site of N_2 occurs on Fe, W, Ni, and Ti metals of FeMo, MoW, NiMo, and TiMo dimers. Because of the different work functions of the dual metals, the electron enrichment of Fe, W, Ni, and Ti sites is promoted by accepting electrons from Mo, facilitating the activation of N_2. This can be clearly seen from Table S2. The same amount of charge is lost on Fe, W, Ni, and Ti sites during adsorption of N_2 and N_2H, while Mo transfers 0.43, 0.38, 0.36, and 0.33 electrons to Fe, W, Ni, and Ti during adsorption of N_2H, respectively. In other words, the activity of Mo-based catalysts is enhanced by introducing a second metal (i.e., the synergistic effect of dual-metal sites).

In general, three typical mechanisms have been proposed for the NRR process, which are known as distal, alternating, and enzymatic mechanisms (Figure 3a), and all the possible intermediates and reaction processes are included. For end-on adsorption, the conversion of N_2 to NH_3 follows either an alternating or distal mechanism, while the enzymatic pathway exhibits a different feature starting from N_2 adsorption with a side-on pattern. Figure 3b summarizes the PDS and limiting potential of NRR on M1M2/g-C_3N_4. Among all the 11 DACs, the PDS of 4 DACs (MnCo/g-C_3N_4, MnFe/g-C_3N_4, CoNi/g-C_3N_4 and FeNi/g-C_3N_4) is the first protonation step of *N_2 + ($H^+ + e^-$) → *N_2H (Figure S3), and the PDS of other 6 DACs (TiMo/g-C_3N_4, TiCr/g-C_3N_4, NiMo/g-C_3N_4, MoW/g-C_3N_4, TiMn/g-C_3N_4 and CrW/g-C_3N_4) is the final protonation step of *NH_3NH_2 + ($H^+ + e^-$) → *NH_3 (Figure S4). In contrast, FeMo/g-C_3N_4 shows a different PDS of *NHNH + ($H^+ + e^-$)

https://dx.doi.org/10.1021/acscentsci.0c00552
ACS Cent. Sci. 2020, 6, 1762−1771

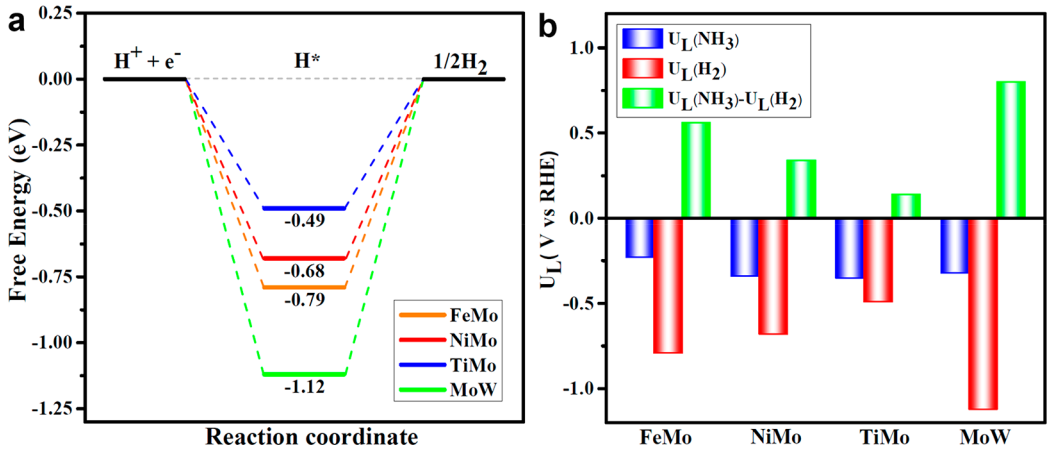

Figure 4. (a) Free energy diagrams of HER on FeMo/g-C_3N_4, NiMo/g-C_3N_4, TiMo/g-C_3N_4, and MoW/g-C_3N_4. (b) Limiting potentials for HER $U_L(H_2)$, NRR $U_L(NH_3)$, and the difference between them $U_L(NH_3) - U_L(H_2)$ on these four catalysts.

→ *NH_2NH (Figure S5) with a relatively low negative limiting potential value of −0.23 V among all the 11 DACs. The excellent activity of FeMo/g-C_3N_4 dual-metal catalyst can be ascribed to the electron-accepting and -donating ability of the dual metal active center as well as a moderate adsorption strength with N-species.

The free energy diagrams along the NRR process for FeMo/g-C_3N_4, TiMo/g-C_3N_4, MoW/g-C_3N_4, and NiMo/g-C_3N_4 are shown in Figures 3c−d and S6. The key intermediates for each elementary step are summarized in Figure S7. It is noteworthy that for most studied transition metal based catalysts, the first protonation step of *N_2 + (H^+ + e^-) → *N_2H is normally a thermodynamically uphill step,[40] while the process for the targeted systems in this work can be exothermic in cases of FeMo/g-C_3N_4 (−0.38 eV), MoW/g-C_3N_4 (−0.20 eV), and NiMo/g-C_3N_4 (−0.02 eV). For TiMo/g-C_3N_4, although the first protonation step is endothermic (0.33 eV), there is a significant reduction in the free energy barrier for the rate-limiting *N_2H formation step due to the stabilization of *N_2H by the dual metals.

In the case of TiMo/g-C_3N_4, MoW/g-C_3N_4, and NiMo/g-C_3N_4, the sixth protonation step of *NH_2 + (H^+ + e^-) → *NH_3 serves as PDS instead of the first protonation process. The calculated free energy barriers of PDS on MoW/g-C_3N_4, NiMo/g-C_3N_4, and TiMo/g-C_3N_4 are 0.32, 0.34, and 0.35 eV, respectively. Therefore, these four heteronuclear DACs of FeMo/g-C_3N_4, NiMo/g-C_3N_4, MoW/g-C_3N_4, and TiMo/g-C_3N_4 exhibit superior catalytic activity of NRR with relatively small negative limiting potentials, which are much lower than their monometal counterparts as well as other similar DACs from previous studies.[13,37,42,43]

Moreover, except for the high catalytic activity, Fe- and Mo-based catalysts also benefit from other merits such as nontoxicity and low price.[44−49] The MoMo and FeFe homonuclear dual metals anchored on g-C_3N_4 monolayer were investigated for comparison. Figure S8 presents the optimized structures of MoMo/g-C_3N_4 and FeFe/g-C_3N_4, and the corresponding free energy diagrams and various intermediates for NRR. The PDS of MoMo/g-C_3N_4 and FeFe/g-C_3N_4 are calculated to be 0.47 and 1.01 eV, which are higher than that of FeMo/g-C_3N_4, TiMo/g-C_3N_4, MoW/g-C_3N_4, and NiMo/g-C_3N_4, indicating that multiple active centers of heteronuclear DACs can reduce the PDS of NRR more efficiently. Note that the above conclusions have been drawn based on a computational hydrogen electrode model, in which the hydrogen bonding between the water and reaction intermediates and the net surface charge is not explicitly considered. These effects may affect the chemical reactivity and product selectivity as found in CO_2RR.[50,51] Note that the hydrogen bonding between the water and reaction intermediates in NRR can greatly improve the yield rate of NH_3 and the Faradaic efficiency and suppress the HER performance.[52]

Additionally, HER, the major competing reaction in NRR, which normally affects the Faradaic efficiency for NRR largely, should also be considered. We thus carried out investigation on the free energy of HER on these four selected catalysts. The H* structures of adsorption site and corresponding free energy HER diagrams are depicted in Figure S9 and Figure 4a, respectively. The free energy barriers (0.49, 0.68, 0.79, and 1.12 eV) are considerable larger than PDS barriers for NRR (0.35, 0.34, 0.23, and 0.32 eV) on heteronuclear DACs of TiMo/g-C_3N_4, NiMo/g-C_3N_4, FeMo/g-C_3N_4 and MoW/g-C_3N_4. Thus, all these four selected catalysts exhibit an excellent suppression effect on HER during NRR. A comparison of the relative limiting potentials (U_L) for each reaction can provide a qualitative estimation for the competition between them. The difference $U_L(NH_3)-U_L(H_2)$ between NRR and HER in terms of their limiting potentials has been used to estimate the selectivity of NRR. A more positive value indicates a higher selectivity toward NRR over HER.[53] As shown in Figure 4b, all of these four catalysts have positive $U_L(NH_3)-U_L(H_2)$ values, demonstrating their high selectivity toward NRR.

Another side effect of H adsorption on the catalytic surface would be H-poisoning, which would thus block the active sites for NRR. To determine whether the NRR is preferred on these four catalysts, the adsorption energies of *H [E_{ads}(*H)] and *N_2 [E_{ads}(*N_2)] were compared as seen in Figure S10. Obviously, heteronuclear DACs of FeMo/g-C_3N_4, TiMo/g-C_3N_4, and NiMo/g-C_3N_4 possess a stronger adsorption ability for *N_2 than *H, suggesting that the surface concentration of *N_2 is higher than *H. For MoW/g-C_3N_4, the small difference between E_{ads}(*H) and E_{ads}(*N_2) implies coadsorption of *N_2 and *H on the active sites. However, experimental strategies, such as enhancing the pH of the solution by diluting the water concentration and using nonaqueous electrolytes[54,55] can effectively reduce the proton donor activity and suppress the HER on the heteronuclear DACs.

https://dx.doi.org/10.1021/acscentsci.0c00552
ACS Cent. Sci. 2020, 6, 1762−1771

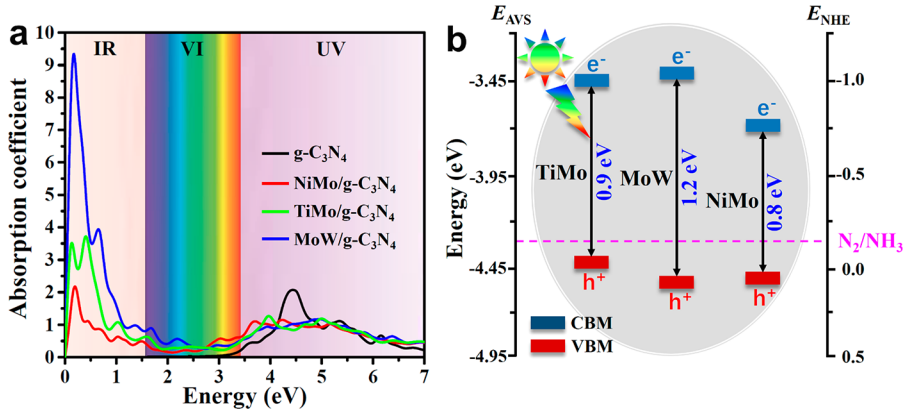

Figure 5. (a) Optical absorption spectra of NiMo/g-C_3N_4, MoW/g-C_3N_4, TiMo/g-C_3N_4, and pure g-C_3N_4. (b) Band edge positions of TiMo/g-C_3N_4, MoW/g-C_3N_4, and NiMo/g-C_3N_4. All the calculations are performed by the HSE06 hybrid functional. E_{NHE} and E_{AVS} denote energy levels relative to normal hydrogen electrode (NHE) and absolute vacuum scale (AVS), respectively.

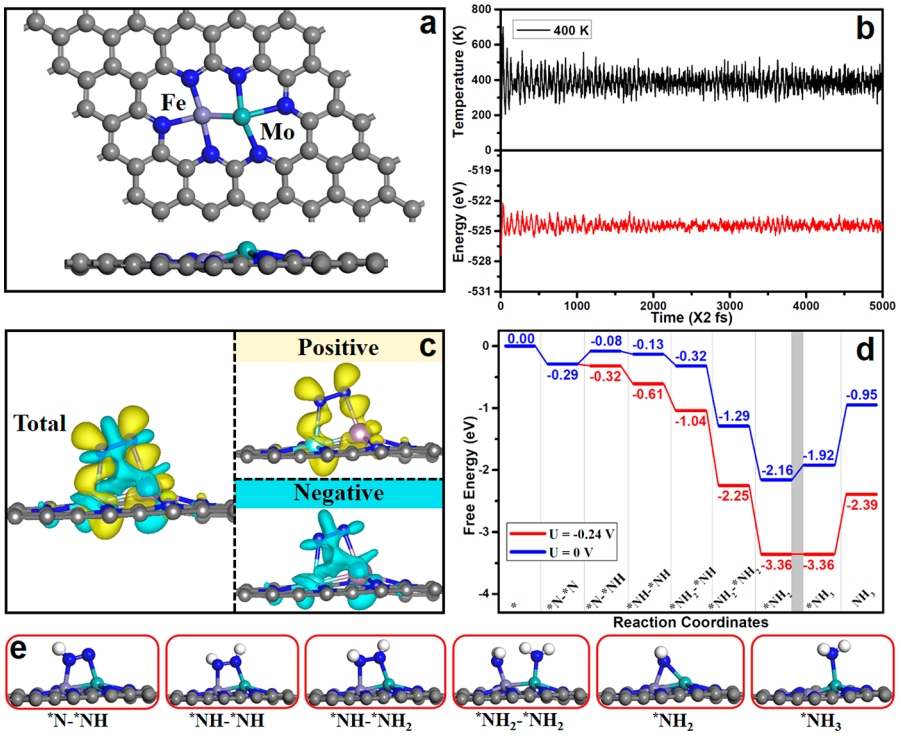

Figure 6. (a) Optimized FeMo/graphene structures. (b) Temperature variations and energy fluctuations versus AIMD simulation time for FeMo/graphene. (c) Charge density difference for N_2 adsorption on FeMo/graphene, where the yellow and cyan indicate the positive and negative charges, respectively. The isosurface value is 0.001 e/Å^3. (d) Free energy diagrams for NRR on FeMo/graphene at different applied potentials, and (e) corresponding configurations of various NRR intermediates. The C, N, H, Mo, and Fe atoms are labeled as gray, blue, white, cyan, and lavender balls, respectively.

The thermal stability of FeMo/g-C_3N_4, NiMo/g-C_3N_4, TiMo/g-C_3N_4, and MoW/g-C_3N_4 was evaluated by AIMD (*ab initio* molecular dynamics) simulations. As evident in Figures S11 and S12, the energy fluctuation along with time evolution oscillates close to the equilibrium state, and the atomic configuration remains stable at 400 K, indicating the high structural stability of these catalysts. The high stability stems from the strong covalent bonds between the dual-metals and the g-C_3N_4 substrate based on the hybridization of metal-3d and N-2p orbitals, and the metal dimers form strong covalent bonds with N atoms at the cavity edge (Figure S13). To get more insights into the kinetic stability of M1M2/g-C_3N_4, we further investigated the minimum energy path for the dissociation of FeMo, MoW, NiMo, and TiMo dimers into two separated monomers. As shown in Figure S14, the calculated diffusion barriers of metal dimers segregated into two individual monomers at two pore sites of a g-C_3N_4 monolayer are 3.14, 3.78, 2.63, and 2.97 eV, respectively, implying that these four DACs of FeMo/g-C_3N_4, MoW/g-C_3N_4, NiMo/g-C_3N_4, and TiMo/g-C_3N_4 have high kinetic stability.

Generally speaking, as a consequence of a relatively large band gap, the g-C_3N_4 monolayer shows weak visible-light absorption.[31,32] The deposition of FeMo, TiMo, MoW, and NiMo dimers on g-C_3N_4 can possibly modify its electronic structure and boost the infrared (IR) and visible (VI) light response. Figure S15 shows the electronic band structures of

https://dx.doi.org/10.1021/acscentsci.0c00552
ACS Cent. Sci. 2020, 6, 1762−1771

FeMo/g-C_3N_4, TiMo/g-C_3N_4, MoW/g-C_3N_4, and NiMo/g-C_3N_4 at the Heyd−Scuseria−Ernzerhof (HSE06) level. The bandgap of the pristine g-C_3N_4 monolayer is 2.7 eV, which agrees with experimental[31] and other theoretical[32] studies. Therefore, it can only absorb the ultraviolet (UV) light. With the deposition of metal dimers, the TiMo/g-C_3N_4, MoW/g-C_3N_4, and NiMo/g-C_3N_4 exhibit semiconducting properties, while FeMo/g-C_3N_4 shows metallic properties (Figure S15). The bandgap of NiMo/g-C_3N_4, TiMo/g-C_3N_4, and MoW/g-C_3N_4 are reduced to 0.8, 0.9, and 1.2 eV, respectively, endowing these catalysts with the ability to capture the VI and IR light. Figure 5a shows that main light absorption peak of pristine g-C_3N_4 lies around 4.50 eV, indicating its strong UV light absorbance and very limited VI light absorbance, consistent with previous studies.[31,32,56] With NiMo, TiMo, and MoW dimers deposited on g-C_3N_4, although the UV light absorbance will be decreased more or less, the VI and IR light absorbances are greatly enhanced due to the decrease of the bandgap value. Therefore, comparing with the pristine g-C_3N_4 monolayer, the selected catalysts are able to harvest VI and IR light with a higher solar conversion efficiency.

To be a good photocatalyst for NRR, besides the satisfactory absorption to sunlight, the semiconductor should have suitable band edge positions that match the N_2/NH_3 potentials.[57−59] As clearly displayed in Figure 5b, the conduction band minimum (CBM) of TiMo/g-C_3N_4, MoW/g-C_3N_4, and NiMo/g-C_3N_4 is higher than the N_2/NH_3 potential, and their valence band maximum (VBM) locate below the N_2/NH_3 potential. The band edge positions indicate that the injected photogenerated electrons on CBM can transfer to adsorbed N_2 for proton coupled electron process effectively, rather than recombine with the holes on VBM. Therefore, comparing with the pure g-C_3N_4, these three DACs are expected to obtain a higher photoconversion efficiency, which ensures photocatalytic performance by the efficient separation of the photoexcited electrons and holes. Hence, we conclude that the above three DACs have the merits of suitable visible light absorption, highly active surface, and suitable band edge positions and may be efficient photocatalysts for NRR.

Above, we have demonstrated that constructing donor−acceptor couples of dual-metal sites is a powerful method to boost NRR. In fact, the generality of this proposed strategy for N_2 activation, i.e., the pull−pull effect based on dual-metal sites to activate the N≡N bond, can also be extended to other 2D porous materials such as g-C_2N,[25,36] phthalocyanine,[26] N-doped graphene,[19−24] and so on. As shown in Figure 6a, the optimized structures of FeMo dual-metal were anchored on N-doped graphene by forming N-coordinated N_3Fe-MoN_3 with an average absorption energy of −6.0 eV per metal atom. The robust thermodynamic stability of FeMo/graphene was further confirmed (see Figures 6b and S16). Charge density difference demonstrates the accumulation and depletion of charge can occur on both sides of N_2 and FeMo (Figure 6c). More importantly, NRR can be achieved for FeMo/graphene through the enzymatic mechanism with a relatively low limiting potential value of −0.24 V (Figure 6d). The first hydrogenation site of N_2 occurs on the Fe site of FeMo metal dimer (Figure 6e), in line with the donor−acceptor couples on M1M2/g-C_3N_4 (Figure 2f). In addition, the free energy for *H adsorption is −0.37 eV (Figure S17), suggesting that the HER can be suppressed by the FeMo bimetallic catalyst.

3. CONCLUSION

In summary, several monolayer g-C_3N_4 supported heteronuclear metal dimers have been designed with excellent activity for NRR. The high activity stems from dual active sites acting synergistically that can potentially break the transition metal-based activity benchmark toward efficient NRR. By evaluating the stability, activity, and selectivity, FeMo/g-C_3N_4, TiMo/g-C_3N_4, MoW/g-C_3N_4, and NiMo/g-C_3N_4 are selected out from 28 candidates as promising catalysts for NRR. Among them, FeMo/g-C_3N_4 exposes a particularly low limiting potential of −0.23 V for NRR and a rather high potential of −0.79 V for HER. Meanwhile, TiMo/g-C_3N_4, MoW/g-C_3N_4, and NiMo/g-C_3N_4 show suitable band edge positions and visible light absorption, which can act as promising photocatalysts for NRR. The design concept of donor−acceptor couples of dual-metal sites is also applicable to other multielectron reactions such as ORR and CO_2RR, which will inspire intensive experiments and computations to further explore other chemical reactions.

4. COMPUTATIONAL DETAILS

Plane-wave density functional theory as implemented in the Vienna Ab Initio Simulation Package (VASP)[60] was used to do all the first-principles spin-polarized calculations with the ion cores described by the projector augmented wave potentials.[61] The Perdew−Burke−Ernzerhof (PBE) functional was used to calculate the electronic exchange-correlation energy within the generalized gradient approximation,[62] and 500 eV was set as the kinetic energy cutoff for the plane-wave basis. 10^{-5} eV was set as the convergence criteria for the energy, and −0.02 eV/Å was set as the convergence criteria for the forces on each atom. A vacuum space of 20 Å was applied in the perpendicular z direction in order to avoid the interaction between two periodic units. The Grimme's semiempirical DFT-D3[63] scheme of dispersion correction was employed to account for the weak interactions. Bader charge analysis was used to evaluate the atomic charge transfer.[64] AIMD simulations carried out under the canonical ensemble lasted for 10 ps. Using the Nóse−Hoover method, the temperature was set to 400 K.[65] Accurate calculations of the electronic band structures and the optical absorption spectra were performed by using the HSE06[66] hybrid functional. The most positive ΔG value (ΔG_{max}) of the whole process was used to obtain the limiting potential U_L by using the equation $U_L = -\Delta G_{max}/e$. Further details of the calculation are provided in the Supporting Information.

■ ASSOCIATED CONTENT

Supporting Information

The Supporting Information is available free of charge at https://pubs.acs.org/doi/10.1021/acscentsci.0c00552.

Details of the calculations of energy difference between adsorption energy (E_b) of metal dimers anchored on g-C_3N_4 and the cohesive energy (E_{coh}) of metal atoms in their crystals; computed the dissolution potential (U_{diss}) of metal-dimers for 28 heteronuclear M1M2/g-C_3N_4; calculated free energy diagrams, the structures of different intermediates; optimized geometries of H* adsorbed; temperature variations and energy fluctuations versus the AIMD simulation time; calculated diffusion energy barriers of metal dimers segregated into two individual monomers at two pore sites of g-C_3N_4;

https://dx.doi.org/10.1021/acscentsci.0c00552
ACS Cent. Sci. 2020, 6, 1762−1771

electronic band structures of pure g-C_3N_4 and M1M2/g-C_3N_4 (PDF)
CIF files of 16 heteronuclear M1M2/g-C_3N_4 (ZIP)

AUTHOR INFORMATION

Corresponding Author

Jinlan Wang − *School of Physics, Southeast University, Nanjing 211189, China;* orcid.org/0000-0002-4529-874X; Email: jlwang@seu.edu.cn

Authors

Shiyan Wang − *School of Physics, Southeast University, Nanjing 211189, China*

Li Shi − *School of Physics, Southeast University, Nanjing 211189, China*

Xiaowan Bai − *School of Physics, Southeast University, Nanjing 211189, China*

Qiang Li − *School of Physics, Southeast University, Nanjing 211189, China*

Chongyi Ling − *School of Physics, Southeast University, Nanjing 211189, China;* orcid.org/0000-0002-4126-9036

Complete contact information is available at: https://pubs.acs.org/10.1021/acscentsci.0c00552

Notes

The authors declare no competing financial interest.

ACKNOWLEDGMENTS

This study was supported financially by the Natural Science Foundation of China (Grant Nos. 21525311, 21703032, and 21773027). The computational resources were provided by the Big Data Computing Center of Southeast University and the National Supercomputers Center at Tianjin.

REFERENCES

(1) Légaré, M.-A.; Bélanger-Chabot, G.; Dewhurst, R. D.; Welz, E.; Krummenacher, I.; Engels, B.; Braunschweig, H. Nitrogen Fixation and Reduction at Boron. *Science* **2018**, *359*, 896−900.

(2) Burford, R. J.; Fryzuk, M. D. Examining the Relationship between Coordination Mode and Reactivity of Dinitrogen. *Nat. Rev. Chem.* **2017**, *1*, 0026.

(3) van der Ham, C. J. M.; Koper, M. T. M.; Hetterscheid, D. G. H. Challenges in Reduction of Dinitrogen by Proton and Electron Transfer. *Chem. Soc. Rev.* **2014**, *43*, 5183−5191.

(4) Zhao, J.; Chen, Z. Single Mo Atom Supported on Defective Boron Nitride Monolayer as an Efficient Electrocatalyst for Nitrogen Fixation: A Computational Study. *J. Am. Chem. Soc.* **2017**, *139*, 12480−12487.

(5) Ling, C.; Niu, X.; Li, Q.; Du, A.; Wang, J. Metal-Free Single Atom Catalyst for N_2 Fixation Driven by Visible Light. *J. Am. Chem. Soc.* **2018**, *140*, 14161−14168.

(6) Yang, X.; Nash, J.; Anibal, J.; Dunwell, M.; Kattel, S.; Stavitski, E.; Attenkofer, K.; Chen, J. G.; Yan, Y.; Xu, B. Mechanistic Insights into Electrochemical Nitrogen Reduction Reaction on Vanadium Nitride Nanoparticles. *J. Am. Chem. Soc.* **2018**, *140*, 13387−13391.

(7) Liu, C.; Li, Q.; Wu, C.; Zhang, J.; Jin, Y.; MacFarlane, D. R.; Sun, C. Single-Boron Catalysts for Nitrogen Reduction Reaction. *J. Am. Chem. Soc.* **2019**, *141*, 2884−2888.

(8) Hao, Y.-C.; et al. Promoting Nitrogen Electroreduction to Ammonia with Bismuth Nanocrystals and Potassium Cations in Water. *Nat. Catal.* **2019**, *2*, 448−456.

(9) Seh, Z. W.; Kibsgaard, J.; Dickens, C. F.; Chorkendorff, I.; Nørskov, J. K.; Jaramillo, T. F. Combining Theory and Experiment in Electrocatalysis: Insights into Materials Design. *Science* **2017**, *355*, eaad4998.

(10) Singh, A. R.; Rohr, B. A.; Schwalbe, J. A.; Cargnello, M.; Chan, K.; Jaramillo, T. F.; Chorkendorff, I.; Nørskov, J. K. Electrochemical Ammonia Synthesis−the Selectivity Challenge. *ACS Catal.* **2017**, *7*, 706−709.

(11) Suryanto, B. H. R.; Du, H.-L.; Wang, D.; Chen, J.; Simonov, A. N.; MacFarlane, D. R. Challenges and Prospects in the Catalysis of Electroreduction of Nitrogen to Ammonia. *Nat. Catal.* **2019**, *2*, 290−296.

(12) Yang, T.; Song, T. T.; Zhou, J.; Wang, S.; Chi, D.; Shen, L.; Yang, M.; Feng, Y. P. High-Throughput Screening of Transition Metal Single Atom Catalysts Anchored on Molybdenum Disulfide for Nitrogen Fixation. *Nano Energy* **2020**, *68*, 104304.

(13) Liu, X.; Jiao, Y.; Zheng, Y.; Jaroniec, M.; Qiao, S.-Z. Building up a Picture of the Electrocatalytic Nitrogen Reduction Activity of Transition Metal Single-Atom Catalysts. *J. Am. Chem. Soc.* **2019**, *141*, 9664−9672.

(14) He, C.; Wu, Z.-Y.; Zhao, L.; Ming, M.; Zhang, Y.; Yi, Y.; Hu, J.-S. Identification of FeN_4 as an Efficient Active Site for Electrochemical N_2 Reduction. *ACS Catal.* **2019**, *9*, 7311−7317.

(15) Hui, L.; Xue, Y.; Yu, H.; Liu, Y.; Fang, Y.; Xing, C.; Huang, B.; Li, Y. Highly Efficient and Selective Generation of Ammonia and Hydrogen on a Graphdiyne-Based Catalyst. *J. Am. Chem. Soc.* **2019**, *141*, 10677−10683.

(16) Geng, Z.; Liu, Y.; Kong, X.; Li, P.; Li, K.; Liu, Z.; Du, J.; Shu, M.; Si, R.; Zeng, J. Achieving a Record-High Yield Rate of 120.9 $\mu gNH_3\ mg^{-1}_{cat.}\ h^{-1}$ for N_2 Electrochemical Reduction over Ru Single-Atom Catalysts. *Adv. Mater.* **2018**, *30*, 1803498.

(17) Ding, C.; Feng, C.; Mei, Y.; Liu, F.; Wang, H.; Dupuis, M.; Li, C. Carbon Nitride Embedded with Transition Metals for Selective Electrocatalytic CO_2 Reduction. *Appl. Catal., B* **2020**, *268*, 118391.

(18) Bhuyan, B.; Devi, M.; Bora, D.; Dhar, S. S.; Newar, R. Design of a Photoactive Bimetallic Cu-Au@G-C_3N_4 Catalyst for Visible Light Driven Hydroxylation of the Benzene Reaction through C−H Activation. *Eur. J. Inorg. Chem.* **2018**, *2018*, 3849−3858.

(19) Zhang, L.; et al. Coordination of Atomic Co−Pt Coupling Species at Carbon Defects as Active Sites for Oxygen Reduction Reaction. *J. Am. Chem. Soc.* **2018**, *140*, 10757−10763.

(20) Hunter, M. A.; Fischer, J. M. T. A.; Yuan, Q.; Hankel, M.; Searles, D. J. Evaluating the Catalytic Efficiency of Paired, Single-Atom Catalysts for the Oxygen Reduction Reaction. *ACS Catal.* **2019**, *9*, 7660−7667.

(21) Wang, J.; et al. Synergistic Effect of Well-Defined Dual Sites Boosting the Oxygen Reduction Reaction. *Energy Environ. Sci.* **2018**, *11*, 3375−3379.

(22) Wang, J.; et al. Design of N-Coordinated Dual-Metal Sites: A Stable and Active Pt-Free Catalyst for Acidic Oxygen Reduction Reaction. *J. Am. Chem. Soc.* **2017**, *139*, 17281−17284.

(23) Zhang, G.; et al. A General Route Via Formamide Condensation to Prepare Atomically Dispersed Metal−Nitrogen−Carbon Electrocatalysts for Energy Technologies. *Energy Environ. Sci.* **2019**, *12*, 1317−1325.

(24) Lu, Z.; et al. An Isolated Zinc−Cobalt Atomic Pair for Highly Active and Durable Oxygen Reduction. *Angew. Chem.* **2019**, *131*, 2648−2652.

(25) Huang, Q.; Liu, H.; An, W.; Wang, Y.; Feng, Y.; Men, Y. Synergy of a Metallic Nico Dimer Anchored on a C_2N−Graphene Matrix Promotes the Electrochemical CO_2 Reduction Reaction. *ACS Sustainable Chem. Eng.* **2019**, *7*, 19113−19121.

(26) Guo, X.; Gu, J.; Lin, S.; Zhang, S.; Chen, Z.; Huang, S. Tackling the Activity and Selectivity Challenges of Electrocatalysts toward the Nitrogen Reduction Reaction Via Atomically Dispersed Biatom Catalysts. *J. Am. Chem. Soc.* **2020**, *142*, 5709−5721.

(27) Hu, R.; Li, Y.; Zeng, Q.; Wang, F.; Shang, J. Bimetallic Pairs Supported on Graphene as Efficient Electrocatalysts for Nitrogen Fixation: Search for the Optimal Coordination Atoms. *ChemSusChem* **2020**, *13*, 3636−3644.

(28) Xue, Z.-H.; Zhang, S.-N.; Lin, Y.-X.; Su, H.; Zhai, G.-Y.; Han, J.-T.; Yu, Q.-Y.; Li, X.-H.; Antonietti, M.; Chen, J.-S. Electrochemical Reduction of N_2 into NH_3 by Donor−Acceptor Couples of Ni and Au

Nanoparticles with a 67.8% Faradaic Efficiency. *J. Am. Chem. Soc.* **2019**, *141*, 14976−14980.
(29) Zhang, J.; Chen, Y.; Wang, X. Two-Dimensional Covalent Carbon Nitride Nanosheets: Synthesis, Functionalization, and Applications. *Energy Environ. Sci.* **2015**, *8*, 3092−3108.
(30) Chen, Z.; Zhao, J.; Cabrera, C. R.; Chen, Z. Computational Screening of Efficient Single-Atom Catalysts Based on Graphitic Carbon Nitride ($G\text{-}C_3N_4$) for Nitrogen Electroreduction. *Small Methods* **2019**, *3*, 1800368.
(31) Wang, X.; Maeda, K.; Thomas, A.; Takanabe, K.; Xin, G.; Carlsson, J. M.; Domen, K.; Antonietti, M. A Metal-Free Polymeric Photocatalyst for Hydrogen Production from Water under Visible light. *Nat. Mater.* **2009**, *8*, 76−80.
(32) Du, A.; et al. Hybrid Graphene and Graphitic Carbon Nitride Nanocomposite: Gap Opening, Electron−Hole Puddle, Interfacial Charge Transfer, and Enhanced Visible Light Response. *J. Am. Chem. Soc.* **2012**, *134*, 4393−4397.
(33) Wang, Y.; Wang, X.; Antonietti, M. Polymeric Graphitic Carbon Nitride as a Heterogeneous Organocatalyst: From Photochemistry to Multipurpose Catalysis to Sustainable Chemistry. *Angew. Chem., Int. Ed.* **2012**, *51*, 68−89.
(34) Dong, G.; Zhang, Y.; Pan, Q.; Qiu, J. A Fantastic Graphitic Carbon Nitride ($G\text{-}C_3N_4$) Material: Electronic Structure, Photocatalytic and Photoelectronic Properties. *J. Photochem. Photobiol., C* **2014**, *20*, 33−50.
(35) Wang, S.; Wei, W.; Lv, X.; Huang, B.; Dai, Y. W Supported on G-CN Manifests High Activity and Selectivity for N_2 Electroreduction to NH_3. *J. Mater. Chem. A* **2020**, *8*, 1378−1385.
(36) Ouyang, Y.; Shi, L.; Bai, X.; Li, Q.; Wang, J. Breaking Scaling Relations for Efficient CO_2 Electrochemical Reduction through Dual-Atom Catalysts. *Chem. Sci.* **2020**, *11*, 1807−1813.
(37) Qian, Y.; Liu, Y.; Zhao, Y.; Zhang, X.; Yu, G. Single Vs Double Atom Catalyst for N_2 Activation in Nitrogen Reduction Reaction: A DFT Perspective. *EcoMater.* **2020**, *2*, e12014.
(38) Ling, C.; Ouyang, Y.; Li, Q.; Bai, X.; Mao, X.; Du, A.; Wang, J. A General Two-Step Strategy−Based High-Throughput Screening of Single Atom Catalysts for Nitrogen Fixation. *Small Methods* **2019**, *3*, 1800376.
(39) Fernandez, E. M.; et al. Scaling Relationships for Adsorption Energies on Transition Metal Oxide, Sulfide, and Nitride Surfaces. *Angew. Chem., Int. Ed.* **2008**, *47*, 4683−4686.
(40) Skúlason, E.; Bligaard, T.; Gudmundsdóttir, S.; Studt, F.; Rossmeisl, J.; Abild-Pedersen, F.; Vegge, T.; Jónsson, H.; Nørskov, J. K. A Theoretical Evaluation of Possible Transition Metal Electro-Catalysts for N_2 reduction. *Phys. Chem. Chem. Phys.* **2012**, *14*, 1235−1245.
(41) Wang, P.; Chang, F.; Gao, W.; Guo, J.; Wu, G.; He, T.; Chen, P. Breaking Scaling Relations to Achieve Low-Temperature Ammonia Synthesis through LiH-Mediated Nitrogen Transfer and Hydrogenation. *Nat. Chem.* **2017**, *9*, 64−70.
(42) Zhang, L.; Zhao, W.; Zhang, W.; Chen, J.; Hu, Z. $Gt\text{-}C_3N_4$ Coordinated Single Atom as an Efficient Electrocatalyst for Nitrogen Reduction Reaction. *Nano Res.* **2019**, *12*, 1181−1186.
(43) Ma, D.; Zeng, Z.; Liu, L.; Huang, X.; Jia, Y. Computational Evaluation of Electrocatalytic Nitrogen Reduction on Tm Single-, Double-, and Triple-Atom Catalysts (TM = Mn, Fe, Co, Ni) Based on Graphdiyne Monolayers. *J. Phys. Chem. C* **2019**, *123*, 19066−19076.
(44) Ashida, Y.; Arashiba, K.; Nakajima, K.; Nishibayashi, Y. Molybdenum-Catalysed Ammonia Production with Samarium Diiodide and Alcohols or Water. *Nature* **2019**, *568*, 536−540.
(45) Cheng, H.; Ding, L.-X.; Chen, G.-F.; Zhang, L.; Xue, J.; Wang, H. Molybdenum Carbide Nanodots Enable Efficient Electrocatalytic Nitrogen Fixation under Ambient Conditions. *Adv. Mater.* **2018**, *30*, 1803694.
(46) Piascik, A. D.; Li, R.; Wilkinson, H. J.; Green, J. C.; Ashley, A. E. Fe-Catalyzed Conversion of N_2 to $N(SiMe_3)_3$ Via an Fe-Hydrazido Resting State. *J. Am. Chem. Soc.* **2018**, *140*, 10691−10694.
(47) Liu, J.-C.; Ma, X.-L.; Li, Y.; Wang, Y.-G.; Xiao, H.; Li, J. Heterogeneous Fe_3 Single-Cluster Catalyst for Ammonia Synthesis Via an Associative Mechanism. *Nat. Commun.* **2018**, *9*, 1610.
(48) Cheng, H.; Cui, P.; Wang, F.; Ding, L.-X.; Wang, H. High Efficiency Electrochemical Nitrogen Fixation Achieved with a Lower Pressure Reaction System by Changing the Chemical Equilibrium. *Angew. Chem., Int. Ed.* **2019**, *58*, 15541−15547.
(49) Qin, B.; Li, Y.; Zhang, Q.; Yang, G.; Liang, H.; Peng, F. Understanding of Nitrogen Fixation Electro Catalyzed by Molybdenum−Iron Carbide through the Experiment and Theory. *Nano Energy* **2020**, *68*, 104374.
(50) Kim, D.; Shi, J.; Liu, Y. Substantial Impact of Charge on Electrochemical Reactions of Two-Dimensional Materials. *J. Am. Chem. Soc.* **2018**, *140*, 9127−9131.
(51) Zhao, X.; Liu, Y. Unveiling the Active Structure of Single Nickel Atom Catalysis: Critical Roles of Charge Capacity and Hydrogen Bonding. *J. Am. Chem. Soc.* **2020**, *142*, 5773−5777.
(52) Wang, M.; Liu, S.; Qian, T.; Liu, J.; Zhou, J.; Ji, H.; Xiong, J.; Zhong, J.; Yan, C. Over 56.55% Faradaic Efficiency of Ambient Ammonia Synthesis Enabled by Positively Shifting the Reaction Potential. *Nat. Commun.* **2019**, *10*, 341.
(53) Montoya, J. H.; Tsai, C.; Vojvodic, A.; Nørskov, J. K. The Challenge of Electrochemical Ammonia Synthesis: A New Perspective on the Role of Nitrogen Scaling Relations. *ChemSusChem* **2015**, *8*, 2180−2186.
(54) Suryanto, B. H. R.; Kang, C. S. M.; Wang, D.; Xiao, C.; Zhou, F.; Azofra, L. M.; Cavallo, L.; Zhang, X.; MacFarlane, D. R. Rational Electrode−Electrolyte Design for Efficient Ammonia Electrosynthesis under Ambient Conditions. *ACS Energy Lett.* **2018**, *3*, 1219−1224.
(55) Zhou, F.; Azofra, L. M.; Ali, M.; Kar, M.; Simonov, A. N.; McDonnell-Worth, C.; Sun, C.; Zhang, X.; MacFarlane, D. R. Electro-Synthesis of Ammonia from Nitrogen at Ambient Temperature and Pressure in Ionic Liquids. *Energy Environ. Sci.* **2017**, *10*, 2516−2520.
(56) Gao, G.; Jiao, Y.; Waclawik, E. R.; Du, A. Single Atom (Pd/Pt) Supported on Graphitic Carbon Nitride as an Efficient Photocatalyst for Visible-Light Reduction of Carbon Dioxide. *J. Am. Chem. Soc.* **2016**, *138*, 6292−6297.
(57) Lv, X.; Wei, W.; Li, F.; Huang, B.; Dai, Y. Metal-Free B@G-CN: Visible/Infrared Light-Driven Single Atom Photocatalyst Enables Spontaneous Dinitrogen Reduction to Ammonia. *Nano Lett.* **2019**, *19*, 6391−6399.
(58) Li, J.; Liu, P.; Tang, Y.; Huang, H.; Cui, H.; Mei, D.; Zhong, C. Single-Atom $Pt\text{−}N_3$ Sites on the Stable Covalent Triazine Framework Nanosheets for Photocatalytic N_2 Fixation. *ACS Catal.* **2020**, *10*, 2431−2442.
(59) Bian, S.; Wen, M.; Wang, J.; Yang, N.; Chu, P. K.; Yu, X.-F. Edge-Rich Black Phosphorus for Photocatalytic Nitrogen Fixation. *J. Phys. Chem. Lett.* **2020**, *11*, 1052−1058.
(60) Kresse, G.; Furthmüller, J. Efficient Iterative Schemes for Ab Initio Total-Energy Calculations Using a Plane-Wave Basis Set. *Phys. Rev. B: Condens. Matter Mater. Phys.* **1996**, *54*, 11169−11186.
(61) Blöchl, P. E. Projector Augmented-Wave Method. *Phys. Rev. B: Condens. Matter Mater. Phys.* **1994**, *50*, 17953−17979.
(62) Perdew, J. P.; Chevary, J. A.; Vosko, S. H.; Jackson, K. A.; Pederson, M. R.; Singh, D. J.; Fiolhais, C. Atoms, Molecules, Solids, and Surfaces: Applications of the Generalized Gradient Approximation for Exchange and Correlation. *Phys. Rev. B: Condens. Matter Mater. Phys.* **1992**, *46*, 6671−6687.
(63) Burns, L. A.; Vazquez-Mayagoitia, A.; Sumpter, B. G.; Sherrill, C. D. Density-Functional Approaches to Noncovalent Interactions: A Comparison of Dispersion Corrections (DFT-D), Exchange-Hole Dipole Moment (XDM) Theory, and Specialized Functionals. *J. Chem. Phys.* **2011**, *134*, No. 084107.
(64) Henkelman, G.; Arnaldsson, A.; Jónsson, H. A Fast and Robust Algorithm for Bader Decomposition of Charge Density. *Comput. Mater. Sci.* **2006**, *36*, 354−360.
(65) Nosé, S. A Unified Formulation of the Constant Temperature Molecular Dynamics Methods. *J. Chem. Phys.* **1984**, *81*, 511−519.

https://dx.doi.org/10.1021/acscentsci.0c00552
ACS Cent. Sci. 2020, 6, 1762−1771

(66) Heyd, J.; Scuseria, G. E.; Ernzerhof, M. Hybrid Functionals Based on a Screened Coulomb Potential. *J. Chem. Phys.* **2003**, *118*, 8207−8215.

https://dx.doi.org/10.1021/acscentsci.0c00552
ACS Cent. Sci. 2020, 6, 1762−1771